Simulation of *XXZ* Spin Models Using Sideband Transitions in Trapped Bosonic Gases

Anjun Chu,[1,2,*] Johannes Will,[3] Jan Arlt,[4] Carsten Klempt,[3,5] and Ana Maria Rey[1,2]
[1]*JILA, NIST and Department of Physics, University of Colorado, Boulder, Colorado 80309, USA*
[2]*Center for Theory of Quantum Matter, University of Colorado, Boulder, Colorado 80309, USA*
[3]*Institut für Quantenoptik, Leibniz Universität Hannover, Welfengarten 1, D-30167 Hannover, Germany*
[4]*Center for Complex Quantum Systems, Department of Physics and Astronomy, Aarhus University, Ny Munkegade 120, DK-8000 Aarhus C, Denmark*
[5]*Institut für Satellitengeodäsie und Inertialsensorik, Deutsches Zentrum für Luft-und Raumfahrt e.V., Welfengarten 1, D-30167 Hannover, Germany*

(Received 6 April 2020; revised 16 September 2020; accepted 27 October 2020; published 7 December 2020)

We theoretically propose and experimentally demonstrate the use of motional sidebands in a trapped ensemble of ^{87}Rb atoms to engineer tunable long-range *XXZ* spin models. We benchmark our simulator by probing a ferromagnetic to paramagnetic dynamical phase transition in the Lipkin-Meshkov-Glick model, a collective *XXZ* model plus additional transverse and longitudinal fields, via Rabi spectroscopy. We experimentally reconstruct the boundary between the dynamical phases, which is in good agreement with mean-field theoretical predictions. Our work introduces new possibilities in quantum simulation of anisotropic spin-spin interactions and quantum metrology enhanced by many-body entanglement.

DOI: 10.1103/PhysRevLett.125.240504

Quantum simulation of iconic models of quantum magnetism in highly controllable atomic systems is emerging as a promising way to gain new insights into fundamental many-body phenomena in condensed matter physics [1], and as a pathway to shed light onto exciting new phenomena in nonequilibrium many-body spin arrays [2–7]. In recent years, rapid progress in the simulation of quantum spin models has been made by taking advantage of the diversity of interactions in ultracold quantum systems, including contact interactions in the motional ground state of ultracold atomic gases [6,8], dipolar interactions in polar molecules [9], magnetic atoms [10–12] and Rydberg atoms [13], as well as long-range interactions in trapped ions [14] and cavity QED systems [7,15–18] mediated by phonon and photon respectively.

One promising avenue in this direction is the fact that nondegenerate thermal gases interacting via purely contact interactions, can emulate spin models by mapping the single-particle energy eigenstates onto a lattice in mode space [5,19–21]. This mapping has been shown to be a powerful way to emulate long-range interacting spin models featuring large many-body energy gaps that have enabled significant enhancement of coherence time [22–24]. Nevertheless, the tunability of the spin model parameters has so far been mainly accomplished by the use of Feshbach resonances, and the atom loss associated with the latter imposes a trade-off between tunability and coherence time [5,25].

In this Letter, we theoretically propose and experimentally demonstrate the use of motional sidebands in a thermal trapped gas of ^{87}Rb atoms to engineer long-range *XXZ* spin models with tunable spin couplings. We benchmark our simulator by probing a dynamical phase transition (DPT) between ferromagnetic and paramagnetic phases in the collective *XXZ* model plus additional transverse and longitudinal fields (also known as the Lipkin-Meshkov-Glick (LMG) model [2,7,26,27]) via Rabi spectroscopy. We experimentally reconstruct the boundary of the dynamical phases by varying atom density and longitudinal field strength and show good agreement with mean-field theoretical predictions. At the end we also discuss the further applications of our scheme in entanglement-enhanced metrology [28–30], as well as generalizations to a wide range of quantum systems.

We consider an ensemble of thermal ^{87}Rb atoms confined in a 3D harmonic trap and prepared in the magnetically insensitive clock states $|\downarrow\rangle \equiv |F=1, m_F=0\rangle$ and $|\uparrow\rangle \equiv |F=2, m_F=0\rangle$. The contact interaction in this two-component bosonic gas can be written in the following second quantized form [31,32],

$$H_{\rm int} = \sum_{\sigma\sigma'=\uparrow,\downarrow} \frac{U_{\sigma\sigma'}}{2} \int d^3\mathbf{R}\, \psi_\sigma^\dagger(\mathbf{R})\psi_{\sigma'}^\dagger(\mathbf{R})\psi_{\sigma'}(\mathbf{R})\psi_\sigma(\mathbf{R}), \quad (1)$$

where $U_{\sigma\sigma'} = 4\pi\hbar^2 a_{\sigma\sigma'}/m$ is the interaction strength between atoms of spin σ and σ', parametrized by the s-wave scattering lengths, $a_{\uparrow\uparrow} = 94.55a_0$, $a_{\uparrow\downarrow} = 98.09a_0$, $a_{\downarrow\downarrow} = 100.76a_0$ [33]. The bosonic field operator $\psi_\sigma(\mathbf{R})$, is expanded in the eigenmode basis of the 3D harmonic trap, $\psi_\sigma(\mathbf{R}) = \sum_{\mathbf{n}} a_{\mathbf{n}\sigma}\phi_{\mathbf{n}}(\mathbf{R})$, where $a_{\mathbf{n}\sigma}$ annihilates a boson of spin σ in eigenmode $\mathbf{n} = \{n^X, n^Y, n^Z\}$ of the harmonic trap, with corresponding wave function $\phi_{\mathbf{n}}(\mathbf{R})$.

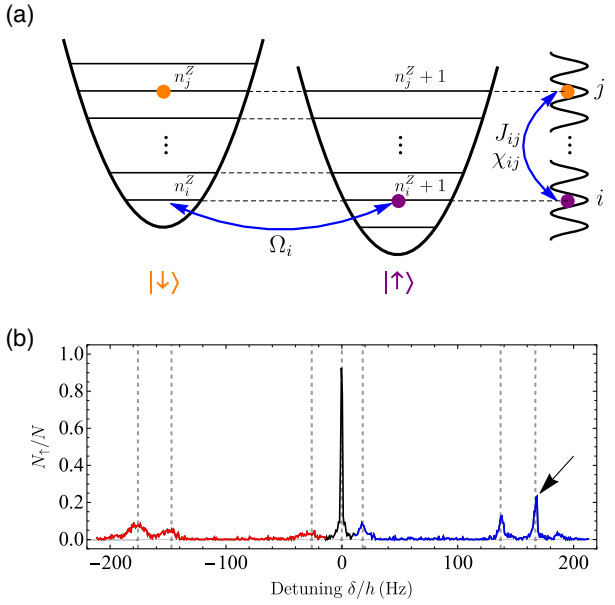

FIG. 1. Simulating XXZ spin models using sideband transitions in a thermal bosonic gas confined in a 3D harmonic trap. (a) Schematic of the effective 3D mode-space lattice for blue Z sideband (only the projection along the Z direction is shown for simplicity). The states $|\Uparrow_i\rangle \equiv |\uparrow; n_i^X, n_i^Y, n_i^Z+1\rangle$ and $|\Downarrow_i\rangle \equiv |\downarrow; n_i^X, n_i^Y, n_i^Z\rangle$, which are the ones coupled by the Raman pulse with Rabi frequency Ω_i, can be regarded as the two spin states pinned at the ith site of the effective 3D mode-space lattice. Contact interactions in bosonic gases generate long-range XXZ couplings J_{ij}, χ_{ij} between lattice sites i and j in mode space (see text). (b) Rabi spectrum in the resolved sideband limit for mean atom density $n = 2.0 \times 10^{12}$ cm^{-3}. The black (blue, red) line represents carrier (blue sideband, red sideband) transitions. Our experiment focuses on the strongest sideband pointed out by the arrow. It is worth mentioning that the suppression of red sideband transitions is related to the anharmonic corrections in optical dipole traps, also observed in Ref. [35].

We understand and analyze the many-body dynamics through a mapping of the single-particle eigenstates of the 3D harmonic trap onto a 3D lattice in mode space, as depicted in Fig. 1(a). Notice that a blue sideband transition along the Z direction couples the following two states in the harmonic trap, $|\Uparrow_i\rangle \equiv |\uparrow; n_i^X, n_i^Y, n_i^Z+1\rangle$ and $|\Downarrow_i\rangle \equiv |\downarrow; n_i^X, n_i^Y, n_i^Z\rangle$. So we can visualize the states $|\Uparrow_i\rangle$ and $|\Downarrow_i\rangle$ as two spin states localized at site i in an effective 3D mode-space lattice. The wave functions associated with $|\Uparrow_i\rangle$ and $|\Downarrow_i\rangle$ states are denoted as $\phi_i^{\Uparrow}(\mathbf{R})$ and $\phi_i^{\Downarrow}(\mathbf{R})$, respectively. Similar treatments can apply to blue sideband transitions along other directions, carrier transitions as well as red sideband transitions [34].

Since we are interested in the collisionless regime of a trapped atomic ensemble, where the trapping potential is much larger than the interaction strength, we assume that each atom is fixed in the mode-space lattice [5,19–21], and that the only relevant process between two colliding atoms is to either remain in the same internal states or to exchange them. Furthermore, we can restrict our discussions to include either empty or singly-occupied lattice sites since the ^{87}Rb gas temperature is above quantum degeneracy [34]. These approximations map the contact interaction term in the Hamiltonian [see Eq. (1)] to a spin-1/2 long-range XXZ model in the mode-space lattice:

$$H_{\rm int} = \sum_{ij} J_{ij} \mathbf{S}_i \cdot \mathbf{S}_j + \sum_{ij} \chi_{ij} S_i^z S_j^z + \sum_i B_i S_i^z. \quad (2)$$

Here, the spin operators can be written in terms of bosonic operators on each lattice site, $\mathbf{S}_i = \sum_{\alpha\beta=\Uparrow,\Downarrow} a_{i\alpha}^\dagger \boldsymbol{\sigma}_{\alpha\beta} a_{i\beta}/2$, where $\boldsymbol{\sigma}_{\alpha\beta}$ are Pauli matrices, and $a_{i\beta}$ annihilates a boson of spin β on lattice site i. The XXZ interaction parameters are given by $J_{ij} = V_{ij}^{\rm ex} U_{\uparrow\downarrow}$, $\chi_{ij} = V_{ij}^{\Uparrow\Uparrow} U_{\uparrow\uparrow} + V_{ij}^{\Downarrow\Downarrow} U_{\downarrow\downarrow} - V_{ij}^{\Uparrow\Downarrow} U_{\uparrow\downarrow} - V_{ij}^{\rm ex} U_{\uparrow\downarrow}$, and $B_i = \sum_{j\neq i} (V_{ij}^{\Uparrow\Uparrow} U_{\uparrow\uparrow} - V_{ij}^{\Downarrow\Downarrow} U_{\downarrow\downarrow})$, and are set by the overlap integral of the relevant 3D harmonic oscillator wave functions: $V_{ij}^{\alpha\beta} = \int d^3\mathbf{R} [\phi_i^\alpha(\mathbf{R})]^2 [\phi_j^\beta(\mathbf{R})]^2$, and $V_{ij}^{\rm ex} = \int d^3\mathbf{R} \phi_i^{\Uparrow}(\mathbf{R}) \phi_i^{\Downarrow}(\mathbf{R}) \phi_j^{\Uparrow}(\mathbf{R}) \phi_j^{\Downarrow}(\mathbf{R})$. The tunability of spin-spin couplings depends on these overlap integrals. For carrier transitions we have $\phi_i^{\Uparrow}(\mathbf{R}) = \phi_i^{\Downarrow}(\mathbf{R}) = \langle \mathbf{R} | n_i^X, n_i^Y, n_i^Z \rangle$, and therefore $V_{ij}^{\alpha\beta} = V_{ij}^{\rm ex}$, making the XXZ spin model equivalent to the isotropic Heisenberg model ($J_{ij} \gg \chi_{ij}$). For the sideband transitions, the wave functions are not the same for the two spin components (e.g., for the blue Z-sideband $\phi_i^{\Downarrow}(\mathbf{R}) = \langle \mathbf{R} | n_i^X, n_i^Y, n_i^Z \rangle$ and $\phi_i^{\Uparrow}(\mathbf{R}) = \langle \mathbf{R} | n_i^X, n_i^Y, n_i^Z + 1 \rangle$), and therefore the overlap integrals are no longer equal. This allows us to have larger Ising couplings χ_{ij}.

In addition to the interaction term, there are extra transverse and longitudinal fields generated by the interrogating laser. For blue sideband transitions, the single-particle Hamiltonian can be written as $H_{\rm sp} = \sum_i [\Omega_i S_i^x - (\delta - \hbar\omega) S_i^z]$, where Ω_i is the mode-dependent Rabi frequency, δ is the laser detuning from the carrier transition, and ω is the relevant trapping frequency. Both $H_{\rm sp}$ and $H_{\rm int}$ [see Eq. (2)] contribute to the dynamics in our XXZ simulator ($H_{XXZ} = H_{\rm sp} + H_{\rm int}$), and the dynamics can be restricted to the fully symmetric Dicke manifold to the leading order. In this limit our model simplifies to the Lipkin-Meshkov-Glick (LMG) model [26],

$$H_{\rm LMG} = \chi S^z S^z + \Omega S^x - \tilde{\delta} S^z. \quad (3)$$

Here, $\tilde{\delta} = \delta - \hbar\omega - B$ is the effective longitudinal field, χ, Ω, and B are the thermal-averaged value of χ_{ij}, Ω_i, and B_i respectively, and $S^{x,y,z} = \sum_i S_i^{x,y,z}$ are the collective spin operators.

The LMG model features interesting spin dynamics, including a ferromagnetic to paramagnetic dynamical phase transition (DPT) [2,7,27]. In general terms, a DPT is

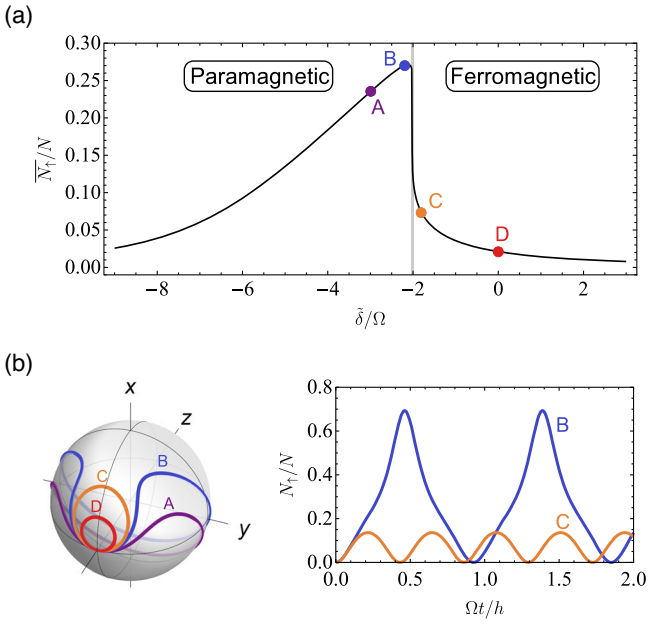

FIG. 2. (a) Dynamical phase transition (DPT) in LMG model with $N\chi/\Omega = 5$, indicated by the sharp behavior in longtime average excitation fraction $\overline{N_\uparrow}/N$. The critical point is marked by the vertical gray line at $\tilde{\delta}/\Omega = -2.02$, separating the dynamical paramagnetic phase (left) and the dynamical ferromagnetic phase (right). (b) Mean-field dynamics of the LMG model with $\tilde{\delta}/\Omega = -3$ (A), -2.2 (B), -1.8 (C), 0 (D). The left panel shows the mean-field trajectories on the Bloch sphere, and the right panel presents the mean-field evolution of the excitation fraction for trajectory B and C. The sharp change in dynamics between trajectory B and C also signals the DPT.

characterized by the existence of a critical point separating phases with distinct dynamical properties in many-body systems. The analog of thermodynamic order parameters is found in longtime average observables, which have a nonanalytic dependence on system parameters. To observe the DPT we initialize all the atoms in the $|\downarrow\rangle$ state, which is the ground state of LMG model when $\tilde{\delta} \to -\infty$, and then perform a sudden quench of the longitudinal field to its final value $\tilde{\delta}$.

In this case, the DPT is signaled by a sharp change in behavior of the longtime average excitation fraction, $\overline{N_\uparrow}/N = \lim_{T\to\infty}(1/T)\int_0^T N_\uparrow(t)/N$, which serves as an order parameter and distinguishes two dynamical phases [see Fig. 2(a)]: A dynamical ferromagnetic phase characterized by $\overline{N_\uparrow}/N \approx 0$, where the vanishing excitation fraction persists even when the final longitudinal field $\tilde{\delta}$ is varied, and a dynamical paramagnetic phase, where $\overline{N_\uparrow}/N$ dynamically adjusts itself following the change of the final longitudinal field $\tilde{\delta}$.

To analyze the DPT we derive mean-field equations of motion for the collective spin operators. They are given by

$$\frac{d}{dt}\mathbf{s} = \mathbf{b} \times \mathbf{s}, \qquad \mathbf{b} = (\Omega, 0, N\chi s^z - \tilde{\delta}), \tag{4}$$

where $s^{x,y,z} = 2\langle S^{x,y,z}\rangle/N$ are the normalized expectation values of collective spin operators. As shown in [34], Eq. (4) can be further reduced to $(\dot{s}^z)^2/2 + V(s^z) = 0$ by eliminating s^x and s^y, and we can relate the DPT with an abrupt change in the number of real roots of the effective potential $V(s^z)$ in this form. The abrupt change in $V(s^z)$ gives rise to distinct properties in spin dynamics shown in Fig. 2(b): The ferromagnetic phase features small oscillations near south pole (trajectory C), while the paramagnetic phase exhibits large excursions that precess around the x axis (trajectory B). The DPT can also be tuned by varying the interaction strength as shown in Fig. 3(d). In the interaction dominant regime ($N\chi/\Omega > 8\sqrt{3}/9$), the DPT generates a second order critical line [marked by the black solid line in Fig. 3(d)] that distinguishes the two dynamical phases. On the other hand, the transition evolves into a smooth crossover region in the weakly interacting regime [$N\chi/\Omega < 8\sqrt{3}/9$, below the black dashed line in Fig. 3(d)], where instead the dynamics is dominated by single particle Rabi flopping.

We experimentally realize the XXZ spin model in a cloud of ^{87}Rb atoms, which is prepared at a temperature of 375(25) nK in a crossed-beam optical dipole trap with trapping frequencies of 143, 21.5, and 171 Hz. This setting ensures the validity of the key approximations in our spin model, including the collisionless regime and a negligible number of doubly occupied modes (below 1.4% for 10^5 atoms) [34]. The atomic ensemble is initialized with a variable mean density n from 0.46 to 4.8×10^{12} cm^{-3} (atom number N from 0.33 to 3.4×10^5), and the atom densities are calibrated by the collisional frequency shift of the carrier transition (-0.48 Hz/10^{12} cm^{-3} [23]). To ensure an unperturbed cloud temperature for different atom densities, an adjustable spin rotation is performed, which partially transfers atoms from the $|\uparrow\rangle$ to the $|\downarrow\rangle$ state and a subsequent removal of the $|\uparrow\rangle$ atoms. The coherent drive between two clock states with resolved motional levels is realized by two copropagating Raman beams focused into the atomic cloud with a 39 μm beam waist. The beams are offset from the trap center in order to drive the first-order motional sidebands [34]. The typical Rabi spectrum of our system is depicted in Fig. 1(b). Here, we focus on the strongest blue sideband at $\omega/2\pi = 171$ Hz. Considering the mean Ising couplings ($N\chi/h \approx 4.63$ Hz/10^{12} cm$^{-3} \times n$) and the mean Rabi frequency ($\Omega/h \approx 0.56$ Hz) for this sideband, our XXZ simulator lies in the interaction dominant regime, where the mentioned DPT is predicted to occur. Instead of direct measurements of the longtime-averaged excitation fraction, which is inevitably limited by technical challenges (e.g., collisional dephasing and atom loss), the order parameter $\overline{N_\uparrow}/N$ is estimated by measuring the excitation fraction at a probe time $t_f = 0.5$ s for fixed Rabi frequency. The entire phase diagram is then obtained by scanning the two-photon

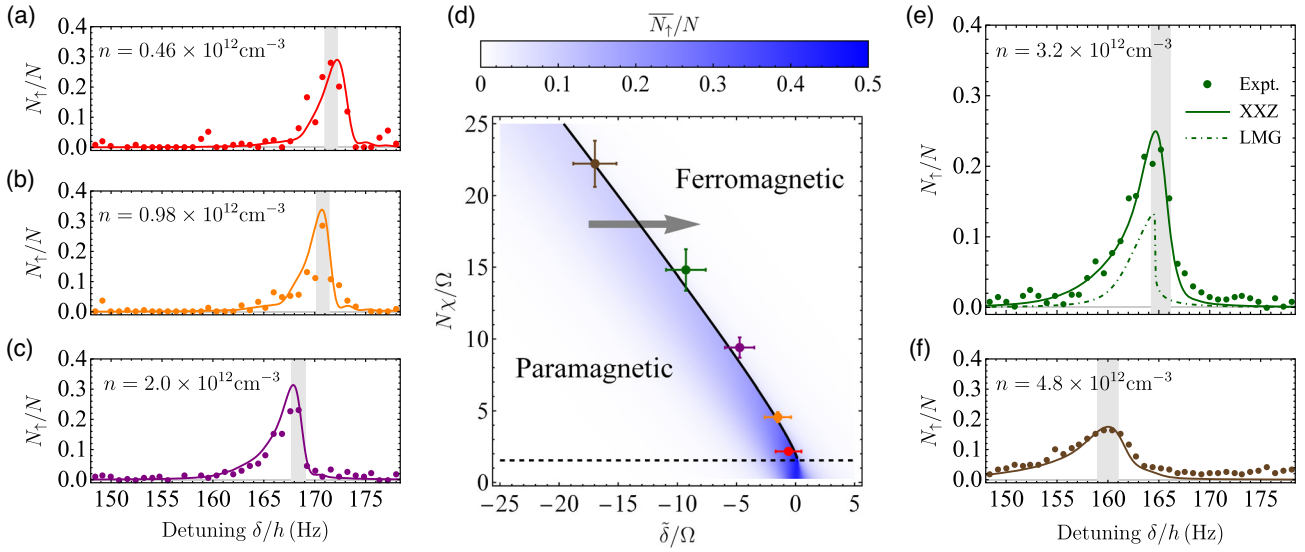

FIG. 3. (a)–(c),(e),(f) Dynamical phase transition in the 171 Hz blue sideband with mean atom density $n = \{0.46, 0.98, 2.0, 3.2, 4.8\} \times 10^{12}$ cm^{-3}, indicated by the asymmetric line shape after evolution time 0.5 s. The shaded areas indicate the critical points, where the uncertainty is set by finite frequency step of detuning as well as fluctuations in atom density and Rabi frequency. The filled circles denote experimental data, the solid lines denote mean-field theoretical predictions by H_{XXZ}, and the green dot-dashed line in (e) denotes the order parameter $\overline{N_\uparrow}/N$ predicted by H_{LMG} (see text). We do not directly add the experimental error bars to the line shape data in (a)–(c),(e),(f) for visual reasons, and the typical statistical uncertainty in each figure is $\Delta N_\uparrow/N = \{0.038, 0.020, 0.013, 0.010, 0.011\}$, respectively. (d) Phase diagram for ferromagnetic to paramagnetic dynamical phase transition. The black solid line denotes the sharp phase boundary of DPT, the black dashed line separates the smooth crossover regime (below) with DPT regime (above), and the gray arrow illustrates the probing direction on phase diagram. The phase boundary is reconstructed from the critical points in (a)–(c),(e),(f) using the same choice of color to label data points.

detuning δ in 0.8 Hz steps and by varying interactions using different atom densities.

The recorded asymmetric line shapes for different atom densities are shown in Figs. 3(a)–3(c), 3(e), 3(f), which is in good agreement with the mean-field theoretical predictions by H_{XXZ} [34]. In Fig. 3(e), we also compare the experimental observation with the order parameter $\overline{N_\uparrow}/N$ (green dot-dashed line) predicted by H_{LMG} [see Eq. (3)]. We find that the recorded line shape captures the two dynamical phases in the LMG model: if we increase the two-photon detuning δ, the slow increase of $N_\uparrow/N$ below resonance indicates the paramagnetic phase, while the sharp change back to $N_\uparrow/N \approx 0$ above resonance indicates the ferromagnetic phase. Compared to the critical behavior of $\overline{N_\uparrow}/N$ in the LMG model, the recorded line shapes are broadened by the inhomogeneous couplings but retain the sharp features associated with the DPT. The inhomogeneities also lead to modifications of effective interaction strength in experiment compared to the LMG model, which can be accounted for by scaling χ by a factor of 0.56. By interpreting the experimentally observed resonant frequencies (obtained from maximal population transfer) as a signature of the critical point of the DPT, we reconstruct the phase boundary between these two dynamical phases [see Fig. 3(d)], which agrees with the theoretical prediction.

To further verify the existence of a DPT with inhomogeneous couplings, we present numerical simulations of mean-field evolution under H_{XXZ} with mean atom density $n = 3.2 \times 10^{12}$ cm^{-3} in Fig. 4. As the detuning is scanned

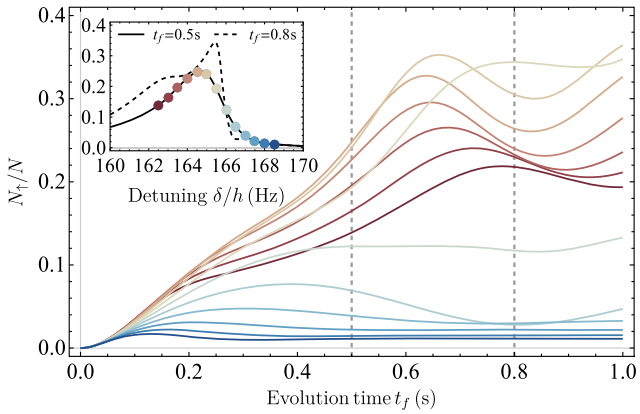

FIG. 4. Numerical simulation of mean-field evolution under H_{XXZ} with mean atom density $n = 3.2 \times 10^{12}$ cm^{-3}. The lines with a color gradient from red to blue show the dynamical behavior from red to blue detuning with 0.5 Hz frequency steps. A sharp change in the excited atom fraction can be observed as the system approaches the critical point. The inset compares two line shapes taken at different evolution times.

from below to above the critical point (marked by a color gradient from red to blue), the excitation fraction $N_\uparrow(t)/N$ features a sharp change in dynamical behavior at the critical detuning, validating the existence of a DPT under our experimental conditions. Compared to the LMG model, we observe damping in the oscillation amplitude of excitation fraction for the inhomogeneous case. To understand the role of the damping, in the inset of Fig. 4 we compare the line shapes at evolution times of $t_f = 0.5$ s (see also Fig. 3) and $t_f = 0.8$ s. Although we see variations in the line shapes computed at these two evolution times (the latter is sharper than the former), both of them consistently display clear signatures of the DPT up to a 1 Hz shift in resonant frequency, which nevertheless lies within the experimental error bars. This analysis justifies the use of $N_\uparrow/N$ evaluated at $t_f = 0.5$ s as a good proxy for the longtime-averaged order parameter.

In summary, we have demonstrated the use of motional sidebands in trapped bosonic gases as a tool to simulate long-range XXZ spin models. A practical application of the demonstrated sideband protocol is the dynamical generation of spin squeezing, a well known feature of the LMG model [30] which makes it useful for enhanced sensing. Although further control of inhomogeneities will be required to observe squeezing in the current setup, we expect spin squeezing can be in reach in the next generation of experiments [34]. Moreover, we expect our protocol can be feasibly implemented in a wide range of experiments, including atomic systems in optical lattices. In these systems the SU(2) symmetry of superexchange interactions could be broken into a XXZ spin model via motional sideband spectroscopy, thanks to the larger tunneling rates of excited bands.

We thank Itamar Kimchi and Diego Barberena for useful discussions. The theoretical work is supported by the AFOSR Grant No. FA9550-18-1-0319, by the DARPA (funded via ARO) Grant No. W911NF-16-1-0576, the ARO single investigator Grant No. W911NF-19-1-0210, the NSF PHY1820885, NSF JILA-PFC PHY-1734006 and NSF QLCI-2016244 grants, and by NIST. The experimental work is funded by the Deutsche Forschungsgemeinschaft (DFG, German Research Foundation) under Germany's Excellence Strategy–EXC-2123 QuantumFrontiers–390837967, and through CRC 1227 (DQ-mat), project A02. J. A. acknowledges support by the Villum Foundation, the Carlsberg Foundation, and the Danish National Research Foundation through the Center of Excellence "CCQ" (Grant No. DNRF156).

*anjun.chu@colorado.edu

[1] A. Auerbach, *Interacting Electrons and Quantum Magnetism* (Springer-Verlag, New York, 1994).
[2] J. Zhang, G. Pagano, P. W. Hess, A. Kyprianidis, P. Becker, H. Kaplan, A. V. Gorshkov, Z.-X. Gong, and C. Monroe, Nature (London) **551**, 601 (2017).
[3] H. Bernien, S. Schwartz, A. Keesling, H. Levine, A. Omran, H. Pichler, S. Choi, A. S. Zibrov, M. Endres, M. Greiner, V. Vuletić, and M. D. Lukin, Nature (London) **551**, 579 (2017).
[4] P. Jurcevic, H. Shen, P. Hauke, C. Maier, T. Brydges, C. Hempel, B. P. Lanyon, M. Heyl, R. Blatt, and C. F. Roos, Phys. Rev. Lett. **119**, 080501 (2017).
[5] S. Smale, P. He, B. A. Olsen, K. G. Jackson, H. Sharum, S. Trotzky, J. Marino, A. M. Rey, and J. H. Thywissen, Sci. Adv. **5**, eaax1568 (2019).
[6] H.-X. Yang, T. Tian, Y.-B. Yang, L.-Y. Qiu, H.-Y. Liang, A.-J. Chu, C. B. Dağ, Y. Xu, Y. Liu, and L.-M. Duan, Phys. Rev. A **100**, 013622 (2019).
[7] J. A. Muniz, D. Barberena, R. J. Lewis-Swan, D. J. Young, J. R. K. Cline, A. M. Rey, and J. K. Thompson, Nature (London) **580**, 602 (2020).
[8] C. Gross and I. Bloch, Science **357**, 995 (2017).
[9] J. L. Bohn, A. M. Rey, and J. Ye, Science **357**, 1002 (2017).
[10] N. Q. Burdick, Y. Tang, and B. L. Lev, Phys. Rev. X **6**, 031022 (2016).
[11] S. Baier, M. J. Mark, D. Petter, K. Aikawa, L. Chomaz, Z. Cai, M. Baranov, P. Zoller, and F. Ferlaino, Science **352**, 201 (2016).
[12] S. Lepoutre, J. Schachenmayer, L. Gabardos, B. Zhu, B. Naylor, E. Maréchal, O. Gorceix, A. M. Rey, L. Vernac, and B. Laburthe-Tolra, Nat. Commun. **10**, 1714 (2019).
[13] C. S. Adams, J. D. Pritchard, and J. P. Shaffer, J. Phys. B **53**, 012002 (2019).
[14] C. D. Bruzewicz, J. Chiaverini, R. McConnell, and J. M. Sage, Appl. Phys. Rev. **6**, 021314 (2019).
[15] R. Mottl, F. Brennecke, K. Baumann, R. Landig, T. Donner, and T. Esslinger, Science **336**, 1570 (2012).
[16] M. A. Norcia, R. J. Lewis-Swan, J. R. K. Cline, B. Zhu, A. M. Rey, and J. K. Thompson, Science **361**, 259 (2018).
[17] E. J. Davis, G. Bentsen, L. Homeier, T. Li, and M. H. Schleier-Smith, Phys. Rev. Lett. **122**, 010405 (2019).
[18] Y. Guo, R. M. Kroeze, V. D. Vaidya, J. Keeling, and B. L. Lev, Phys. Rev. Lett. **122**, 193601 (2019).
[19] A. M. Rey, A. V. Gorshkov, and C. Rubbo, Phys. Rev. Lett. **103**, 260402 (2009).
[20] A. M. Rey, A. V. Gorshkov, C. V. Kraus, M. J. Martin, M. Bishof, M. D. Swallows, X. Zhang, C. Benko, J. Ye, N. D. Lemke, and A. D. Ludlow, Ann. Phys. (Amsterdam) **340**, 311 (2014).
[21] A. P. Koller, M. L. Wall, J. Mundinger, and A. M. Rey, Phys. Rev. Lett. **117**, 195302 (2016).
[22] C. Deutsch, F. Ramirez-Martinez, C. Lacroûte, F. Reinhard, T. Schneider, J.-N. Fuchs, F. Piéchon, F. Laloë, J. Reichel, and P. Rosenbusch, Phys. Rev. Lett. **105**, 020401 (2010).
[23] G. Kleine Büning, J. Will, W. Ertmer, E. Rasel, J. Arlt, C. Klempt, F. Ramirez-Martinez, F. Piéchon, and P. Rosenbusch, Phys. Rev. Lett. **106**, 240801 (2011).
[24] C. Solaro, A. Bonnin, F. Combes, M. Lopez, X. Alauze, J.-N. Fuchs, F. Piéchon, and F. Pereira Dos Santos, Phys. Rev. Lett. **117**, 163003 (2016).
[25] A. Widera, S. Trotzky, P. Cheinet, S. Fölling, F. Gerbier, I. Bloch, V. Gritsev, M. D. Lukin, and E. Demler, Phys. Rev. Lett. **100**, 140401 (2008).

[26] H. J. Lipkin, N. Meshkov, and A. Glick, Nucl. Phys. **62**, 188 (1965).
[27] V. Borish, O. Marković, J. A. Hines, S. V. Rajagopal, and M. Schleier-Smith, Phys. Rev. Lett. **124**, 063601 (2020).
[28] D. J. Wineland, J. J. Bollinger, W. M. Itano, F. L. Moore, and D. J. Heinzen, Phys. Rev. A **46**, R6797 (1992).
[29] M. Kitagawa and M. Ueda, Phys. Rev. A **47**, 5138 (1993).
[30] J. Ma, X. Wang, C.-P. Sun, and F. Nori, Phys. Rep. **509**, 89 (2011).
[31] A. Sørensen, L.-M. Duan, J. I. Cirac, and P. Zoller, Nature (London) **409**, 63 (2001).
[32] A. Micheli, D. Jaksch, J. I. Cirac, and P. Zoller, Phys. Rev. A **67**, 013607 (2003).
[33] E. G. M. van Kempen, S. J. J. M. F. Kokkelmans, D. J. Heinzen, and B. J. Verhaar, Phys. Rev. Lett. **88**, 093201 (2002).
[34] See Supplemental Material at http://link.aps.org/supplemental/10.1103/PhysRevLett.125.240504 for details of numerical simulations and experimental techniques, includes Refs. [7,23,28,30,35–40].
[35] B. Allard, M. Fadel, R. Schmied, and P. Treutlein, Phys. Rev. A **93**, 043624 (2016).
[36] Y.-J. Lin, A. R. Perry, R. L. Compton, I. B. Spielman, and J. V. Porto, Phys. Rev. A **79**, 063631 (2009).
[37] G. Reinaudi, T. Lahaye, Z. Wang, and D. Guéry-Odelin, Opt. Lett. **32**, 3143 (2007).
[38] W. Maineult, C. Deutsch, K. Gibble, J. Reichel, and P. Rosenbusch, Phys. Rev. Lett. **109**, 020407 (2012).
[39] A. Kaplan, M. F. Andersen, and N. Davidson, Phys. Rev. A **66**, 045401 (2002).
[40] J. Schachenmayer, A. Pikovski, and A. M. Rey, Phys. Rev. X **5**, 011022 (2015).